Građevinski materijali i konstrukcije
Building Materials and Structures
journal homepage: www.buildingmaterialsstructures.com

https://doi.org/10.5937/GRMK2600026M

Original scientific paper

Hoop stresses in porous thick-walled concrete cylinders using rheological-dynamical analogy and drucker-prager yield criterion

Dragan D. Milašinović[1)], Nataša Mrđa Bošnjak[*2)]

[1)] *Faculty of Civil Engineering Subotica, University of Novi Sad, Kozaračka 2a, 24000 Subotica, Serbia*
[2)] *Faculty of Architecture, Civil Engineering and Geodesy, University of Banja Luka, University City, Bulevar vojvode Petra Bojovića 1A, 78000 Banja Luka, Bosnia and Herzegovina*

Article history
Received: 10 September 2026
Received in revised form: 19 October 2026
Accepted: 30 October 2026
Available online: 20 November 2026

Keywords
rheological-dynamical analogy (RDA),
porosity thresholds,
DP yield criterion,
associated flow rule,
ABAQUS

ABSTRACT

A new iterative method for modeling the inelastic behavior of concrete structures from the elastic range to ultimate loading is presented through an analogy with damped dynamic systems. This analogy simplifies complex nonlinear structural responses into solvable linearized equations that describe viscoelastic-plastic effects. The model predicts the strain hardening rule for concrete. The yield conditions are generalized using the Drucker-Prager (DP) criterion with an associated flow rule. The parameters of the DP criterion are investigated both theoretically and experimentally, with and without considering the influence of porosity. Standard concrete cylinders tested to failure under compression are analyzed for both normal-strength and high-strength concretes. The creep coefficient plays a key role in the viscoelastic-plastic response and in determining porosity thresholds. Thick-walled concrete cylinders are analyzed throughout their service life using the finite element software ABAQUS. Instead of entering the porosity into the software as fixed experimental data, it is generated within the model via boundary energy states. With this step, the analogy becomes a constitutive theory that attempts to explain the micro-mechanics of damage. The main results indicate that the normal cohesive stresses in thick-walled cylinders correspond to hoop stresses and reach their peak values at the elastic limit.

ONLINE FIRST

1 Introduction

In the study of structural components under static loading conditions at normal temperatures, it has generally been accepted that time-rate effects are not important and that conventional plasticity theory adequately models material behavior. However, time-rate effects are always present to some extent in all inelastic deformations, and considerable attention was devoted during the second half of the twentieth century to determining the constitutive relations governing the nonlinear time-dependent behavior of materials. A substantial body of literature is available on this topic, ranging from studies of simple creep behavior [1] to the incorporation of plastic effects through rheological models [2]. By applying the yield criterion, according to which yielding occurs when the portion of stress work that is conserved reaches a certain maximum value, it has been shown that two phenomena follow from the constitutive equation of inelasticity. On the one hand, when the load is constant, yielding may occur after a certain period of creep. On the other hand, when a constant strain rate is applied, the yield stress increases with increasing strain rate. From the early stages of finite element method (FEM) development, this topic motivated the formulation of numerical approaches for studying the inelastic time-dependent behavior of materials, which depends on numerous factors [3–5]. In this context, numerical stability in quasi-static elasto-viscoplastic analysis has been investigated as a key aspect of FEM [6,7].

Many structural materials, particularly at elevated temperatures, exhibit creep and viscoplastic behavior. The former essentially involves a redistribution of stress and/or strain over time under the material's elastic response, whereas the latter refers to time-dependent plastic deformation. Experimental observations cannot readily distinguish between these two phenomena, and their separation has largely been an analytical convenience rather than a physical necessity. Consequently, overlay models for time-dependent nonlinear material analysis have been extensively developed [8,9]. Another situation in which time-rate effects become important is the dynamic loading of structures. For example, experimental evidence shows that the instantaneous yield strength of a material subjected to high strain rates can be significantly greater than the corresponding quasi-static value [5]. In addition to general approaches, special attention has been devoted to the investigation of inelastic time-dependent deformations in

[*] Corresponding author:
E-mail address: natasa.mrdja-bosnjak@aggf.unibl.org

concrete and concrete structures, which remain the dominant construction materials in civil engineering [10,11].

Recent studies on the inelastic behavior of concrete structures subjected to long-term loading have primarily focused on the development and propagation of plastic zones using advanced constitutive models that combine plasticity, damage, and creep effects. Numerous studies employ continuum-based elasto-plastic formulations, such as the DP model or concrete damage plasticity models, to capture the evolution of stress and strain fields in axisymmetric and thick-walled structural elements, including cylinders and pressure vessels [12,13]. In these approaches, the boundary between elastic and plastic regions is typically determined using stress-based creep criteria and time-dependent material parameters. Although some studies account for microstructural degradation or creep-induced softening under sustained loading [14,15], porosity is generally treated as a homogenized material property, without a coupling between local porosity variations and the corresponding local stress state governing the elasto-plastic transition. Therefore, further investigation is needed into how spatial variations in porosity affect the local mechanical response and the transition between elastic and inelastic behaviour in concrete structures.

Previous studies based on the RDA have established the theoretical basis for analysing the inelastic behaviour of concrete and have addressed the influence of porosity on the local mechanical response. In the analysis of thick-walled concrete cylinders subjected to compressive loading up to failure, the local representation of porosity is particularly important because spatial variations in porosity can affect the stress state and the transition between elastic and inelastic behaviour. Unlike approaches that treat porosity as a global or averaged material parameter, an element-wise description enables local variations in porosity to be accounted for in the FEM. Building on previous RDA-based investigations of the relationship between porosity and local stresses, the present study extends this approach by incorporating an iterative procedure in which a complete FEM is performed at each successive RDA iteration. The effects of this procedure on hoop-stress distributions, radial displacements, and the evolution of the elasto-viscoplastic boundary are investigated for porous, thick-walled concrete cylinders.

The aim of this study is to investigate the inelastic behaviour of porous, thick-walled concrete cylinders by applying an iterative procedure within the RDA framework. The procedure combines RDA iterations, the DP yield criterion, and an element-wise description of porosity, with a FEM performed at each iteration. Particular attention is paid to the distribution of hoop stresses, interpreted within the RDA framework as normal cohesive stresses, and to the effects of creep, porosity, and RDA iterations on the predicted mechanical response. Changes in radial displacements and in the position of the elasto-viscoplastic boundary are also examined by comparing porous and non-porous configurations. The principal methodological contribution of this study is the application of the iterative RDA procedure to the FEM of porous concrete cylinders, enabling assessment of the effects of spatially distributed porosity on their inelastic behaviour.

2 Materials and methods using RDA

The RDA provides a theoretical framework for analyzing the deformation behavior, damage accumulation, and failure mechanisms of engineering materials under uniaxial, cyclic, and general stress states [16]. By introducing the concept of critical damping of matter, the RDA framework explains the resonant tuning of all internal processes. Physically, this means that the material is on the border between a dominantly elastic response and a dominantly dissipative response, which directly links critical damping to the onset of damage and fracture, as well as to the material response under harmonic loading through the derivation of the phase angle, cyclic strain amplitude, and the RDA storage and loss moduli, [17], [18]. Milašinović in [17] derived the equation for solid matter established by Bernoulli for an incompressible fluid, considering the passage of the strain energy density through two cross sections. In addition, based on the roots of the quadratic equation corresponding to the positive and negative values of Poisson's ratios, two dynamic stress-strain curves were derived in [19]. Taking into account ref. [20–24], damage variable at the peak of the stress-strain diagram, the intermediate strain and the ultimate strain are defined in [25].

For general stress states, the DP yield criterion is employed [26], whose parameters are correlated with the Mohr-Coulomb (MC) hypothesis. Applying the RDA method, linear and nonlinear cohesion and the angle of internal friction were defined, establishing a functional relationship between the creep coefficient, internal friction angle, cohesion, and damage variable, [27].

Furthermore, a linear dependence of the creep coefficient and the modulus of elasticity on porosity was established in [28], as well as a non-linear influence of porosity on compressive strength, the dynamic Poisson's ratio, strain energy density, and total energy dissipation, considering numerous studies which indicate that the progression of damage or strength degradation in concrete does not follow a linear pattern, [29,30]. Five distinct threshold values for porosity were identified in [28], while accounting for the limitations of classical elasticity theory for materials with a Poisson's ratio of less than 0.2, [31].

The accuracy and reliability of the RDA model were confirmed through the application of the finite strip method to folded-plate structures, [32], as well as through numerical analysis using the FEM in the ABAQUS software—an analysis validated against long-term geodetic measurements conducted on composite timber-concrete beams, [33].

2.1 RDA strain hardening rule

In the case of ideal plastic behavior, the response of a solid body is a straight line. In this case, there is a simple solution without strain hardening. At an intermediate strain ε_E, the material transitions from the elastic to the viscoelastoplastic (VEP) region with a viscous normal stress S_g, where the index g denotes the quasi-static material parameters. It is shown in [27] that the normal viscous stress is a function of the dynamic viscosity and the strain rate, as follows:

$$S_g = \lambda_R \frac{d\varepsilon}{dt} = \frac{f_c \varphi_g}{\Psi_g^{1/2}\left(1+\varphi_g\right)^2} \tag{1}$$

However, it is well known that it is difficult or even impossible to obtain an elastic-plastic solution that provides a complete strain history, from the elastic state to the limit load, using classical methods. In addition, many structural materials exhibit strain-hardening behavior; therefore, analytical expressions for yield curves as quasi-static curves

ONLINE FIRST

are often used. The most commonly used formula for the plasticity of metals is given in [34].

In this work, RDA is applied, which allows the analysis of stress and strain as time-dependent phenomena, including fatigue crack growth and fracture [35,36]. A detailed RDA explanation of the behavior of different types of metals under strain hardening is given in [35], where the strength of VEP materials is defined by the stress:

$$Y = \sigma_c + H'\varepsilon_{vp} \tag{2}$$

where H' denotes the viscoplastic (VP) modulus:

$$H' = \frac{E_H}{i \cdot \varphi_1}, \quad i = 1,\ 2,\ 3,\ ... \tag{3}$$

i denotes the iteration index. In the VEP range, the following creep coefficient applies:

$$\varphi_Y^{(i)} = 1 + i \cdot \varphi_1 \tag{4}$$

whereas the VEP strain is:

$$\varepsilon_Y^{(i)} = \varepsilon_{el}\varphi_Y^{(i)} \tag{5}$$

The increase in strength per iteration is defined as follows:

$$Y^{(i)} = \frac{\sigma_P\left(1+i\varphi_1\right) + \sigma_E\left(1+\varphi_1\right)\left[i\left(1+i\varphi_1\right)-1\right]}{i\varphi_1\left(1+i\varphi_1\right)} \tag{6}$$

If the proportional stress σ_P equals the stress at the elastic limit σ_E, as in the case of quasi-brittle materials, we obtain:

$$Y^{(i)} = \sigma_E \frac{1+i\varphi_1 + \left(1+\varphi_1\right)\left[i\left(1+i\varphi_1\right)-1\right]}{i\varphi_1\left(1+i\varphi_1\right)} \tag{7}$$

For the measured compressive strength of concrete and iteration index $i = 1$, we obtain:

$$Y^{(1)} = \sigma_E \frac{1}{D_1} = f_c \tag{8}$$

Therefore, the uniaxial compressive yield stress of concrete using the RDA method is:

$$\sigma_c^{(i)} = Y^{(i)} D_1^{(i)} \tag{9}$$

This strain-hardening rule for a concrete core confined by a steel tube and subjected to uniaxial compressive loading was confirmed in [37] using experimental data reported in [38]. The comparison was also performed in accordance with Eurocode 4 recommendations and numerically using the FEM in ANSYS software.

Under strain hardening, the RDA modulus decreases, while the yield stress increases with increasing creep coefficient. Another important phenomenon is creep. Namely, if a material is subjected to compressive loading until failure, the VP strain and displacement increase. This also refers to the increase in the damage variable and Poisson's ratio with increasing creep coefficient.

3 Results and Discussion

In this study, the parameters defining the DP yield criterion were investigated theoretically and experimentally for normal-strength concrete (NSC), type N concrete, and high-strength concrete (HSC), type SG concrete. Table 1 shows the mechanical properties of SG concrete, which were analyzed in detail using RDA in [25]. The selected concrete is non-standard, with relatively high strength but also high deformability compared to type N concrete. This is a low-shrinkage, expansive material, commercially known as SikaGrout®-212 (a powder concrete mix consisting of cement, crushed stone aggregate, and powdered cement additives). For comparison, experimental data are given in Table 2 for a mix of N concrete [39]. This type of concrete was analyzed using RDA in [40]. Cylindrical specimens under unconfined compressive stress were analyzed for the case of strain hardening under conditions that can realistically be expected during the service life of the concretes considered.

Table 1. Mechanical properties of an SG concrete cylinder [25]

Quasi-static Poisson's ratio	μ_g	0.2
Creep coefficient	φ_g	0.67
Modulus of elasticity (MPa)	E_H	30994
Compressive strength (MPa)	f_c	65.86
Dry density (kg/m^3)	ρ	2265.5
Analytical quasi-static curve	$\sigma = \frac{1}{2\cdot 0.025344}\left(\sqrt{1+4\cdot 0.025344\cdot 49196.83\cdot\varepsilon}-1\right)$	
Dynamic creep coefficient	$\varphi_1 = \varphi_g + 1$	1.67
Dynamic Poisson's ratio	$\mu_1 = \varphi_1/2\left(1+\varphi_1\right)$	0.31277
Modulus ratio	$\Psi = \left(2+3\varphi_1\right)\Big/\left(2+3\varphi_1+\varphi_1^2\right)$	0.715
Angle of internal friction (°)	$\phi = arc\cos\Psi$	44.331
Maximum cohesion (MPa)	$c_c = \left(f_c\varphi_1\right)\Big/\left(\Psi^{3/2}\left(1+\varphi_1\right)^2\right)$	25.51

ONLINE FIRST

Table 2. Mechanical properties of an N concrete cylinder [39]

Quasi-static Poisson's ratio	μ_g	0.1267
Creep coefficient	φ_g	0.3394
Modulus of elasticity (MPa)	E_H	31800
Compressive strength (MPa)	f_c	35
Dry density (kg/m^3)	ρ	2340
Analytical quasi-static curve	$\sigma = \frac{1}{2 \cdot 0.040066}\left(\sqrt{1+4 \cdot 0.040066 \cdot 42593.08 \cdot \varepsilon}-1\right)$	
Dynamic creep coefficient	$\varphi_1 = \varphi_g + 1$	1.3394
Dynamic Poisson's ratio	$\mu_1 = \varphi_1 / 2\left(1+\varphi_1\right)$	0.28627
Modulus ratio	$\Psi = \left(2+3\varphi_1\right) \Big/ \left(2+3\varphi_1+\varphi_1^2\right)$	0.77
Angle of internal friction (º)	$\phi = arc\cos\Psi$	39.614
Maximum cohesion (MPa)	$c_c = \left(f_c \varphi_1\right) \Big/ \left(\Psi^{3/2}\left(1+\varphi_1\right)^2\right)$	12.67

According to the MC failure criterion, the normal stress σ_n and shear stress τ_n acting on the failure surface satisfy the following relationship:

$$\left|\tau_n\right| = \sigma_n \tan\phi + c_{MC} \tag{10}$$

where c_{MC} is the cohesion of the surface, while ϕ is the angle of internal friction.

The graphical representation of Eq. (10) is a straight line:

$$\frac{\tau_n}{\sigma_n} = \tan\phi + \frac{1}{\tan\alpha} = \frac{1}{\cos\phi} \tag{11}$$

where α is the fracture angle

$$\alpha = 45^\circ + \frac{\phi}{2} \tag{12}$$

For the measured compressive strength f_c, we obtain:

$$\sigma_n = \frac{f_c}{2}\ ,\ c_{MC} = \frac{f_c}{2}\frac{1}{\tan\alpha} \tag{13}$$

Consequently, for the SG concrete cylinder at zero iteration, we obtain:

$$\alpha = 45^\circ + \frac{44.331^\circ}{2} = 67.165^\circ$$

$$c_{MC} = 32.93\frac{1}{2.375} = 13.87 \text{ MPa},$$

$$\frac{\tau_n}{\sigma_n} = \tan\phi + \frac{c_{MC}}{\sigma_n} = 0.9769 + \frac{13.87}{32.93} = 1.398$$

The application of the RDA method begins with the use of Eq. (14), given in [27]:

$$\frac{c_c}{\sigma_n} = \frac{2\varphi_1}{\left(\cos\phi\right)^{3/2}\left(1+\varphi_1\right)^2} \tag{14}$$

$$\frac{c_c}{\sigma_n} = \frac{2 \cdot 1.67}{\left(\cos\left(44.331^\circ\right)\right)^{3/2}\left(1+1.67\right)^2} = 0.7744$$

So, the stress ratio on the failure surface using the RDA method is:

$$\frac{\tau_n}{\sigma_n} = \tan\phi + \frac{c_c}{\sigma_n} = 0.9769 + 0.7744 = 1.75$$

The uniaxial tensile strength at zero iteration is given by Eq. (15):

$$f_t = 2c_c\frac{\cos\phi}{1+\sin\phi} \tag{15}$$

$$f_t = 2 \cdot 25.5\frac{0.715}{1+0.69879} = 21.48 \text{ MPa}.$$

Therefore, the uniaxial tensile yield stress at zero iteration is:

$$\sigma_t = f_t D_1 = 21.48 \cdot 0.6255 = 13.44 \text{ MPa}.$$

3.1 Drucker-prager parameters for associated flow

Plastic work can be expressed in terms of the accumulated effective plastic strain. A generalization of this condition is the associated flow rule, or normality principle, in plasticity theory. The term associated is used because plastic flow is derived from the yield criterion. For the DP circle to coincide with the outer apices of the MC hexagon in any cross-section, it can be shown that the cohesion under plane strain conditions is as follows:

$$d = \frac{3\sqrt{3}c_c}{\sqrt{9+12\tan^2\phi}} \tag{16}$$

The angle of internal friction is:

$$\tan\beta = \frac{3\sqrt{3}\tan\phi}{\sqrt{9+12\tan^2\phi}} \tag{17}$$

ONLINE FIRST

where the quantities c_c and ϕ are defined by the RDA method in [27].

The yield stress in compression under plane strain conditions is:

$$\sigma_c = \frac{d}{1-\frac{1}{3}tan\,\beta} \tag{18}$$

Therefore, for SG concrete at the initial iteration ($i=0$), we obtain:

$$tan\,\beta = \frac{3\sqrt{3}\cdot 0.97688}{\sqrt{9+12\cdot 0.97688^2}} = \frac{5.076}{4.522} = 1.122\,,\ \beta = 48.3^\circ\,,$$

$$d = \frac{3\sqrt{3}\cdot 25.51}{4.522} = 29.3 \text{ MPa},.$$

The stress ratio on the failure surface is:

$$\frac{\tau_n}{\sigma_n} = tan\,\beta + \frac{d}{\sigma_n} = 1.122 + \frac{29.3}{32.93} = 2.01\,,$$

whereas the compressive yield stress is:

$$\sigma_c = \frac{29.3}{1-\frac{1}{3}\cdot 1.122} = 46.82 \text{ MPa}.$$

3.2 Variation of density

The void volume fraction (VVF) at fracture can be described as follows:

$$\text{VVF} = \frac{dV - dV_0}{dV} \tag{19}$$

where dV is the volume of the representative volume element (RVE) at a point in the material, while dV_0 is the volume of the matrix in the RVE. Equation (19) represents the definition of porosity as well as VVF, which is difficult to measure directly. On the other hand, it is quite easy to measure the change in material density of dry samples. Namely, if the initial density and damaged density of the material are denoted by ρ_0 and ρ, respectively, Eq. (19) can be expressed as:

$$\text{VVF} = 1 - \frac{\rho}{\rho_0} \tag{20}$$

Lemaitre and Dufailly in [41] used the change in density between the damaged and initial states in the interpretation of a micromechanical model of a spherical cavity in a spherical RVE to demonstrate the relationship between the damage variable and porosity:

$$D_{LD} = \left(1 - \frac{\rho}{\rho_0}\right)^{2/3} \tag{21}$$

In [28], Milašinović showed that this formula is valid only if the porosity threshold p_{max} is included in Eq. (21).

3.3 Strain hardening rule

The analytical stress-strain curve describing a cylinder strength experiment in a press can be calculated using RDA if the compressive strength, elastic modulus, concrete density, and Poisson's ratio are experimentally determined. This procedure was carried out in [25] on an SG concrete cylinder (cast in standard cylindrical molds with a diameter of 150 mm and a height of 300 mm) at standard age (28 days), whose measured and calculated parameters are shown in Table 1. However, during the service life of the concrete, strain-hardening behavior is expected to evolve from elastic to ductile behavior after the yield stress is reached.

The strain-hardening rule at zero iteration for an SG concrete cylinder yields:

$$D_1 = \frac{\varphi_1}{1+\varphi_1} = \frac{1.67}{1+1.67} = 0.6255\,,$$

$$\sigma_{ef} = \frac{f_c}{1-D_1} = \frac{65.86}{1-0.6255} = 175.89 \text{ MPa},$$

$$\sigma_E = \sigma_c = f_c D_1 = 65.86\cdot 0.6255 = 41.2 \text{ MPa},$$

$$\varepsilon_Y = \varepsilon_{el}\varphi_1 = \frac{41.2}{30994}1.67 = 0.00133\cdot 1.67 = 0.00222\,.$$

From Eqs. (4), (5), and (7), the following is obtained by iteration:

$$\varphi_Y^{(1)} = 2.67\,,\ \varepsilon_Y^{(1)} = \frac{41.2}{30994}2.67 = 0.00133\cdot 2.67 = 0.00355\,,$$

$$Y^{(1)} = \sigma_E\frac{1}{D_1} = f_c = 65.86 \text{ MPa},$$

$$D_1^{(1)} = \frac{2.67}{1+2.67} = 0.7276\,,$$

$$\sigma_c^{(1)} = 65.86\cdot 0.7276 = 47.92 \text{ MPa}$$

$$\varphi_Y^{(2)} = 1+2\cdot 1.67 = 4.34\,,$$

$$\varepsilon_Y^{(2)} = \frac{41.2}{30994}4.34 = 0.00133\cdot 4.34 = 0.00577\,,$$

$$Y^{(2)} = 41.2\frac{1+2\cdot 1.67+(1+1.67)\left[2(1+2\cdot 1.67)-1\right]}{2\cdot 1.67(1+2\cdot 1.67)} = 70.61 \text{ MPa},$$

$$D_1^{(2)} = \frac{4.34}{1+4.34} = 0.8128\,,$$

$$\sigma_c^{(2)} = 70.61\cdot 0.8128 = 57.39 \text{ MPa}$$

$$\varphi_Y^{(3)} = 1+3\cdot 1.67 = 6.01\,,$$

$$\varepsilon_Y^{(3)} = \frac{41.2}{30994}6.01 = 0.00133\cdot 6.01 = 0.00799\,,$$

$$Y^{(3)} = 41.2\frac{1+3\cdot 1.67+(1+1.67)\left[3(1+3\cdot 1.67)-1\right]}{3\cdot 1.67(1+3\cdot 1.67)} = 70.43 \text{ MPa},$$

ONLINE FIRST

$$D_1^{(3)} = \frac{6.01}{1+6.01} = 0.8574\,,$$

$$\sigma_c^{(3)} = 70.43 \cdot 0.8574 = 60.39 \text{ MPa}.$$

Figure 1 shows the stress-strain curves under strain hardening for both analyzed concretes.

Table 3 shows the strain-hardening parameters for SG concrete at zero iteration using the RDA prediction and the DP criterion, while Table 4 shows the parameters for N concrete.

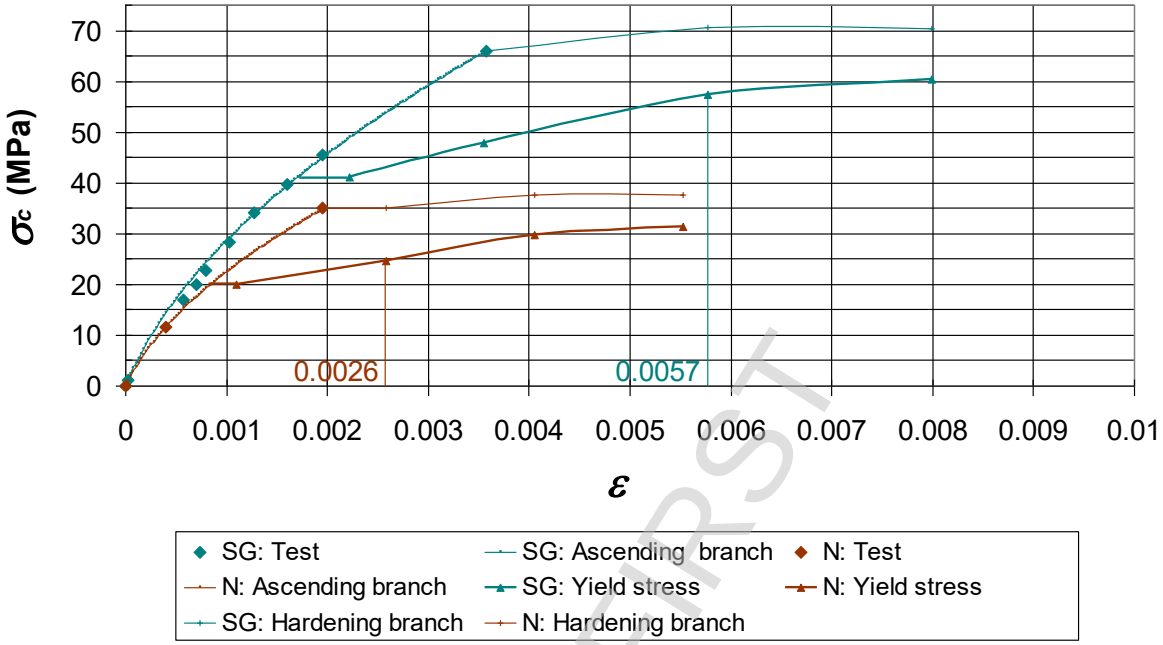


Figure 1. Stress–strain curves due to strain hardening for both analyzed concretes with indicated ultimate strains

Table 3. Strain-hardening parameters for SG concrete at zero iteration

HSC		RDA	DP: associated flow
RDA modulus	E_R (MPa)	11606.28	11606.28
Compressive strength	f_c (MPa)	65.86	65.86
Angle of internal friction	ϕ or β (degree)	44.33	48.3
Cohesion	c_c or d (MPa)	25.5	29.3
Dilatation angle	ψ (degree)	-	48.3
Ratio of the yield stress	K	-	1
Yield stress in compression	σ_c (MPa)	41.2	46.82
Yield stress in tension	σ_t (MPa)	13.43	-
DP parameter	A (MPa)	11.7	-
DP parameter	B	0.293	-

Table 4. Strain-hardening parameters for N concrete at zero iteration

NSC		RDA	DP: associated flow
RDA modulus	E_R (MPa)	13593.23	13593.23
Compressive strength	f_c (MPa)	35	35
Angle of internal friction	ϕ or β (degree)	39.614	46.023
Cohesion	c_c or d (MPa)	12.669	15.863
Dilatation angle	ψ (degree)	-	46.023
Ratio of the yield stress	K	-	1
Yield stress in compression	σ_c (MPa)	20.039	24.235
Yield stress in tension	σ_t (MPa)	6.824	-
DP parameter	A (MPa)	5.878	-
DP parameter	B	0.284	-

ONLINE FIRST

Further, using the strain-hardening rule, results for the first three iterations were obtained for both analyzed concretes. The differences in the parameters obtained using the RDA prediction and the DP criterion for associated flow arise from different assumptions in the two theories. The RDA method follows the strain-hardening rule via a stress-strain curve, while the DP criterion follows associated flow theory. Considering the differences between the two approaches, the agreement in the parameters can be considered very satisfactory.

3.4 Influence of porosity

The strain energy densities, porosity thresholds and the VVF value, were derived in [28] and applied in this paper across the iterations. For the zero iteration in the case of SG concrete, the calculated values are as follows:

W_{el} =0.499308037 MJ/m^3, W_{d1} =0.603418976 MJ/m^3,

W_{d2} =0.347815406 MJ/m^3,

$W_d = W_{d1} - W_{d2}$ =0.25560357 MJ/m^3,

$p_{max} = \dfrac{W_d}{W_{el}}$ =0.512, $p_{min} = \dfrac{2W_{el} - W_{d1} - W_{d2}}{W_{el}}$ =0.095,

$p_f = \dfrac{p_{min}}{p_{max}}$ =0.185, $p_E = \dfrac{W_{d1} - W_{el}}{W_{el}}$ =0.209,

$c_{VVF} = (1-0.6255)13.87 = 5.19$ MPa,

$$\sigma_{VVF} = \frac{5.19 \cdot \left(cos\left(44.33\right)\right)^{3/2} \left(1+1.67\right)^2}{1.67} = 13.41 \text{ MPa},$$

$A = 1.67$,

$$B = 1.67 \cdot 0.209\left(\frac{13.41}{175.89} - 1\right) - 0.512\left(1+1.67-0.6255\right) = -1.369 ,$$

$$C = 0.512\left(1+1.67\right)0.209\left(1 - \frac{13.41}{175.89}\right) = 0.263 ,$$

$$\text{VVF} = \frac{1.369 - \sqrt{1.369^2 - 4 \cdot 1.67 \cdot 0.263}}{2 \cdot 1.67} = 0.309 .$$

Table 5 shows the porosity thresholds and iterations-based values of the VVF for both analyzed concretes.

The porosities p_f controlling the static strength range from 0.14 to 0.25. This is in accordance with what has been reported in [42,43].

One of the key issues in investigating the influence of porosity is the relationship between the value of VVF and the damage variable D_1. The value of VVF is defined over the volume, while the value of D_1 is defined over the cross-sectional area of the cylinder. Figure 2 shows the results for both analyzed concretes. In the case of normal concrete, the ultimate strain of 0.0026 is reached already in the first iteration with a damage variable D_1 of 0.7, which should be considered as critical [44]. In the case of SG concrete, the critical damage variable of 0.81 is reached in the second iteration, when an ultimate strain of 0.0057 is reached. In both analyzed concrete samples, the VVF value increases with the increase in the damage variable D_1 until the ultimate strain is reached.

Table 5. Porosity thresholds and iterations-based values of the VVF

Concrete	p_{max}	p_E	p_f	p_{min}	VVF	D_1	D_{LD}
SG: i=0	0.512	0.209	0.185	0.095	0.309	0.6255	0.6399
SG: i=1	0.623	0.243	0.221	0.138	0.358	0.7276	0.7294
SG: i=2	0.718	0.271	0.246	0.177	0.362	0.8128	0.8021
SG: i=3	0.767	0.286	0.255	0.196	0.358	0.8574	0.8382
N: i=0	0.458	0.191	0.167	0.077	0.265	0.5725	0.5944
N: i=1	0.593	0.234	0.212	0.126	0.35	0.7005	0.7057
N: i=2	0.689	0.262	0.239	0.165	0.363	0.7863	0.78
N: i=3	0.742	0.279	0.25	0.186	0.36	0.8338	0.8194

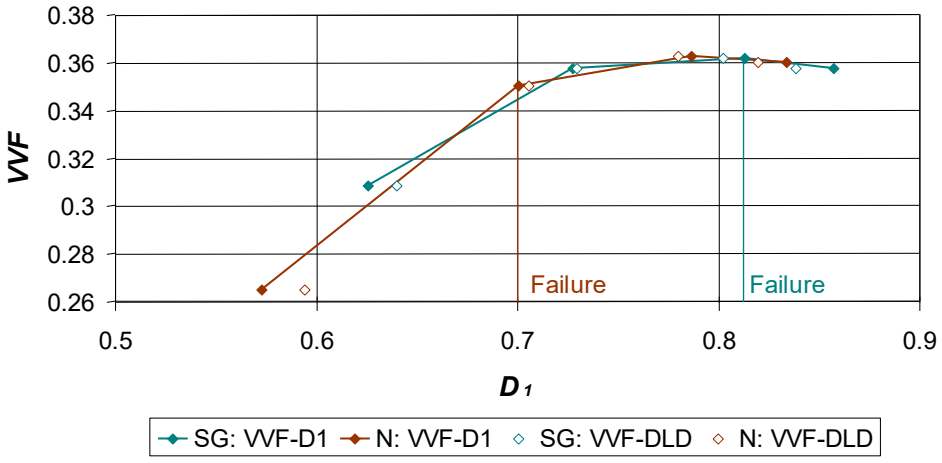


Figure 2. Variations of VVF with respect to both damage variables across iterations

ONLINE FIRST

Figure 2 also shows the results of Eq. (21) for the damage variable D_{LD}, when the maximum porosities $p_{\max}$ are included. The agreement between the results is excellent, considering the completely different assumptions used in deriving the damage variables.

The compressive strengths corresponding to the porosity thresholds are shown in Fig. 3 for SG concrete at zero iteration, while Fig. 4 shows the results for N concrete.

In highly porous materials such as thick-walled concrete cylinders before collapse, the pores are not isolated spherical bubbles, but a network of microscopic "hinged" geometric structures (similar to honeycomb or collapsible lattice structures). When compressed, the internal micro-beams do not expand outward, but collapse (fold) inward, pulling the surrounding material with them. A negative Poisson's ratio in the stiffness matrix is the only way for continuum mechanics (a macro-model) to mathematically describe this purely micro-structural geometric collapse of the porous network. Figure 5 shows the influence of porosity in all iterations for SG concrete, while Fig. 6 shows the results for N concrete. In all iterations for both analyzed concretes, the compressive strengths become zero at values of VVF approximately 0.36, i.e., between the porosity thresholds p_E and p_{max}.

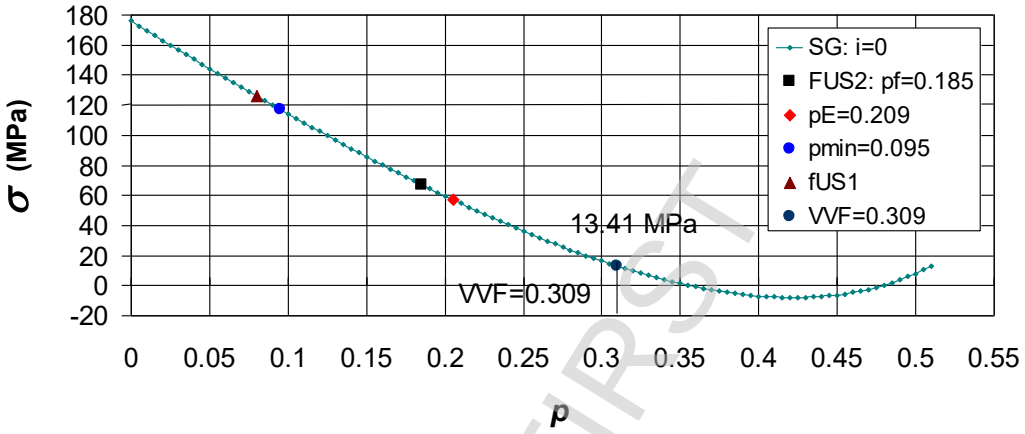


Figure 3. Compressive strengths of SG concrete at zero iteration versus porosity thresholds

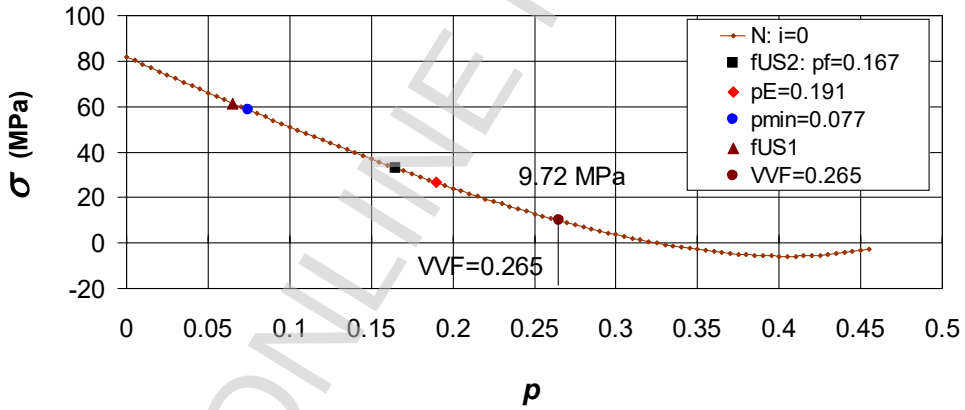


Figure 4. Compressive strengths of N concrete at zero iteration versus porosity thresholds

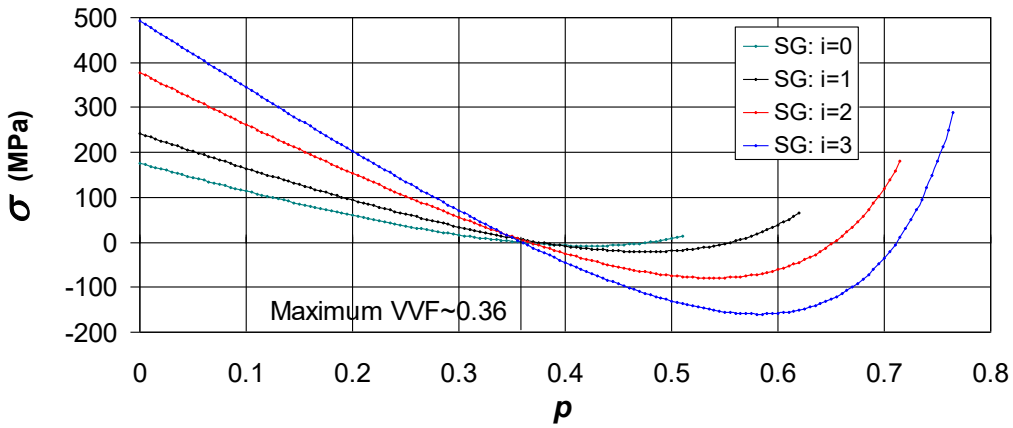


Figure 5. Influence of porosity in all iterations on SG concrete

ONLINE FIRST

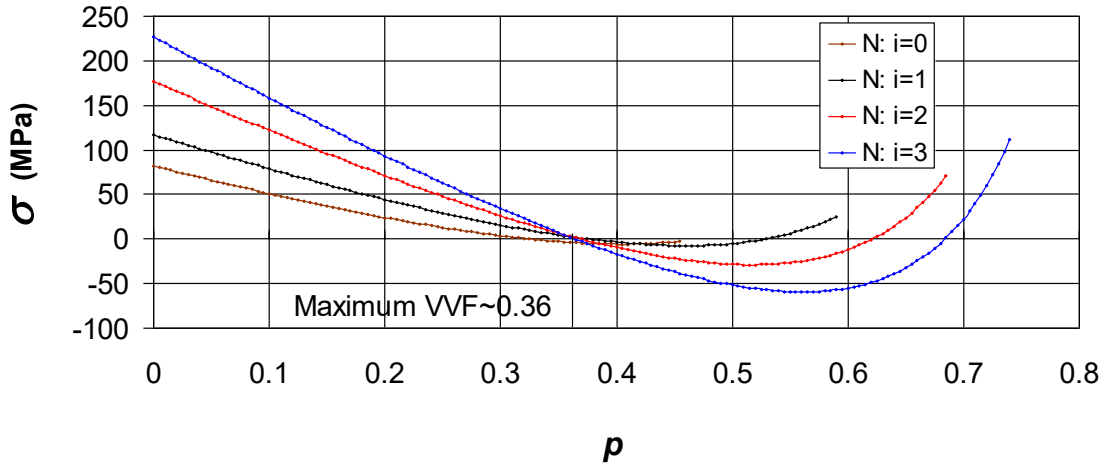


Figure 6. Influence of porosity in all iterations on N concrete

Deriving porosity from the energy densities generated by positive and negative Poisson's ratios dramatically goes beyond simple engineering "mathematical analogy" (where only nonlinear creep is mapped to linear oscillations). When RDA is extended to this level, it actually moves from simple mathematical modeling to fundamental solid-state physics and thermodynamic laws of conservation of mass and energy. RDA is purely kinematics and mechanics (forces, deformations, damping). However, the introduction of strain energy density introduces thermodynamics. The change in porosity is here viewed as a variation in energy density within a dry solid. This transforms the model from a descriptive tool (how concrete creeps) to an energy balance of a material that has micro-voids (porosity).

Let us determine the RDA parameters of SG concrete based on the calculated value of VVF. For zero iteration, we obtain:

$$\varphi_{\text{VVF}} = 1.67\left(1-\frac{0.309}{0.512}\right) = 0.663$$

$$\mu_{\text{VVF}} = \frac{0.663}{2\left(1+0.663\right)} = 0.2$$

$$D_{\text{VVF}} = \frac{0.663}{1+0.663} = 0.399\,,\ \Psi_{\text{VVF}} = \frac{1-0.2-2\cdot 0.2^2}{1-0.2} = 0.9$$

$$\phi_{\text{VVF}} = arccos\left(0.9\right) = 25.842^\circ$$

$$\alpha_{\text{VVF}} = 45^\circ + \frac{25.842^\circ}{2} = 57.921^\circ$$

$$\sigma_{\text{VVF}} = 175.887\left\{1-\frac{0.3087}{0.2085}\left[1-0.6255\left(1-0.3987\right)\right]\right\} = 13.41\ \text{MPa},$$

$$c_{MC,\text{VVF}} = \frac{13.41}{2}\frac{1}{1.595} = 4.2\ \text{MPa},\quad \sigma_{n,\text{VVF}} = \frac{13.41}{2} = 6.705\ \text{MPa}.$$

The stress ratio on the failure surface is:

$$\frac{\tau_{n,\text{VVF}}}{\sigma_{n,\text{VVF}}} = tan\,\phi_{\text{VVF}} + \frac{c_{MC,\text{VVF}}}{\sigma_{n,\text{VVF}}} = 0.484 + \frac{4.2}{6.705} = 1.11\,.$$

The application of the RDA method gives:

$$c_{c,\text{VVF}} = \frac{13.41\cdot 0.663}{\left(0.9\right)^{3/2}\left(1+0.663\right)^2} = 3.76\,\text{MPa},$$

$$\frac{c_{c,\text{VVF}}}{\sigma_{n,\text{VVF}}} = \frac{2\cdot 0.663}{cos\left(25.842^\circ\right)^{3/2}\left(1+0.663\right)^2} = 0.56\,.$$

Therefore, the stress ratio on the failure surface using the RDA method is:

$$\frac{\tau_{n,\text{VVF}}}{\sigma_{n,\text{VVF}}} = tan\,\phi_{\text{VVF}} + \frac{c_{c,\text{VVF}}}{\sigma_{n,\text{VVF}}} = 0.484 + 0.56 = 1.04\,.$$

The application of the DP criterion for associated flow gives:

$$tan\,\beta_{\text{VVF}} = \frac{3\sqrt{3}\cdot 0.484}{\sqrt{9+12\cdot 0.484^2}} = \frac{2.515}{3.437} = 0.73\,,\quad \beta = 36.12^\circ\,,$$

$$d_{\text{VVF}} = \frac{3\sqrt{3}\cdot 3.76}{3.437} = 5.69\ \text{MPa}.$$

Therefore, the stress ratio on the failure surface is:

$$\frac{\tau_{n,\text{VVF}}}{\sigma_{n,\text{VVF}}} = tan\,\beta_{\text{VVF}} + \frac{d_{\text{VVF}}}{\sigma_{n,\text{VVF}}} = 0.73 + \frac{5.69}{6.705} = 1.58\,.$$

Table 6 shows the model parameters by iteration for both analyzed concretes. At zero iteration, the quasi-static behavior of both concretes is evident. Also, the compressive stress decreases with iteration, while the creep coefficient φ_{VVF}—and therefore the strains and displacements—increases. The reason for the decrease in compressive stress is the increase in porosity thresholds with iteration (see Table 5).

Two phenomena observed in metals and other VEP materials have not been linked to a common source until now. These are static fatigue loading leading to creep failure and the increase in yield strength with strain rate. If the quasi-static stress at the limit of elasticity is used in the RDA analysis for the cohesion calculation at zero iteration, we obtain the results shown in Table 1:

$$\sigma_E = \frac{\varphi_g}{K_E^*} = \frac{0.67}{0.025344} = 26.44\ \text{MPa},$$

$$c_{c,\text{VVF}} = \frac{26.44\cdot 0.663}{\left(0.9\right)^{3/2}\left(1+0.663\right)^2} = 7.42\ \text{MPa}.$$

ONLINE FIRST

Table 6. Model parameters based on iteration-based values of the VVF

Concrete	φ_{VVF}	μ_{VVF}	$c_{c,\mathrm{VVF}}$ (MPa)	ϕ_{VVF} ($^\circ$)	σ_{VVF} (MPa)	MC: $\frac{\tau_{n,\mathrm{VVF}}}{\sigma_{n,\mathrm{VVF}}}$	RDA: $\frac{\tau_{n,\mathrm{VVF}}}{\sigma_{n,\mathrm{VVF}}}$	DP: $\frac{\tau_{n,\mathrm{VVF}}}{\sigma_{n,\mathrm{VVF}}}$
SG: i=0	0.663	0.199	3.762	25.74	13.41	1.11	1.04	1.58
SG: i=1	1.136	0.266	2.236	36.17	6.51	1.24	1.42	1.88
SG: i=2	2.153	0.341	1.252	49.76	3	1.55	2.02	2.06
SG: i=3	3.209	0.381	0.757	57.98	1.61	1.89	2.54	2.09
N: i=0	0.564	0.18	2.537	22.97	9.72	1.09	0.95	1.47
N: i=1	0.956	0.244	1.385	32.66	4.28	1.19	1.29	1.79
N: i=2	1.74	0.318	0.847	45.2	2.16	1.42	1.79	2.02
N: i=3	2.58	0.36	0.537	53.55	1.22	1.68	2.23	2.08

The normal cohesive stress is given by Eq. (49).

$$\left|S_{\mathrm{VVF}}\right| = c_{c,\mathrm{VVF}}\cos\phi_{\mathrm{VVF}} = 7.42\cdot\cos\left(25.842^\circ\right) = 6.68 \text{ MPa}.$$

Due to the normal cohesive stress, the compressive strengths are slightly higher than those determined experimentally in quasi-static tests [38], as shown in Fig. 1.

In addition, the experimentally confirmed observation that the instantaneous yield strength of 41.2 MPa (Table 3) under high strain rates is significantly higher than the corresponding quasi-static value of 26.44 MPa is also demonstrated here [5].

3.5 Analysis of porous thick-walled concrete cylinders

The problem under study concerns thick-walled concrete cylinders subjected to gradually increasing internal pressure, with assumed plane stress conditions in the axial direction [7]. The DP yield criterion for associated flow is assumed for which the parameters are defined using the RDA.

The first part of the FEM analysis refers to the influence of creep, without porosity, i.e. VVF, while in the second part VVF is introduced localized by finite elements. The implementation of porosity at the finite element level is based on the relationship between the local stress state and the VVF in each finite element of the structure, as defined in [33].

Based on the stresses obtained from initial FEM analysis at time *t* in ABAQUS, which primarily considers the influence of creep, the porosity for each element is calculated according to RDA. With the obtained porosity values per element, the elastic modulus and Poisson's ratio for each element is then determined through the relationship between elastic modulus and porosity, and creep coefficient and Poisson's ratio. Adjusted elastic moduli were then assigned to each element and the analysis was re-run to obtain a corrected structural response of the cylinder, which includes the effect of porosity under long-term loading.

The inner radius of the analyzed cylinder, denoted as r_1, is 100 mm and the outer radius, denoted as r_2, is 200 mm. Owing to the geometric symmetry of cylinder and the loading conditions, only one quarter of the cylinder cross-section was analyzed, Fig. 7. Appropriate symmetry boundary conditions were applied along the symmetry planes, significantly reducing the number of finite elements and computational time while preserving the accuracy of the solution. The answer is given in cylindrical coordinates (r, θ, z). The FEM discretization was performed using the CPE4R element (A 4-node bilinear plane strain quadrilateral element with reduced integration) available in the ABAQUS element library [45]. A convergence study indicated that the results stabilized with an element size of 1 mm, and the given mesh was adopted for the analysis. The final mesh consisted of 23618 elements.

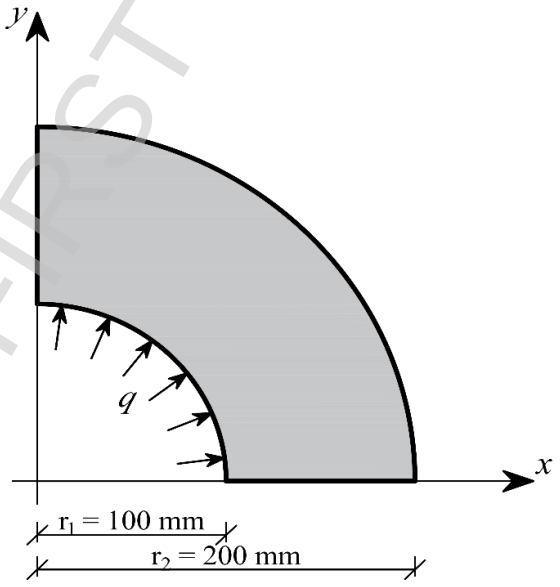


Figure. 7. A quarter of the cross-section of the thick-walled cylinder

The Treska criterion – which can be considered a special case of the MC criterion, with $\phi = 0$ – simply states that a material will yield when a critical level of shear stress is reached:

$$\tau_{max} = \frac{\sigma_1 - \sigma_3}{2} \tag{22}$$

where $\sigma_1 = \sigma_\theta$ and $\sigma_3 = \sigma_r$ are the maximum and minimum principal stresses in thick-walled concrete cylidres. Therefore, plastic deformation occurs without strain hardening under the condition:

$$\sigma_\theta - \sigma_r = 2\cdot q_1 \frac{r_1^2 r_2^2}{r_2^2 - r_1^2}\frac{1}{r^2} = S_g \tag{23}$$

Plastic deformation, which must start from the inner surface of the thick-walled cylinder, with a further increase in internal pressure, gradually spreads towards its unloaded surface, until plastic deformation affects the entire cylinder. The load at which this will occur can be obtained from the

PUBLISHED ONLINE FIRST

following boundary conditions: $r = r_2$, $\sigma_r = 0$; $r = r_1$, $S_g = -q_1$,

$$q_1 = S_g \, ln \frac{r_2}{r_1} \tag{24}$$

Based on expression (1) for SG concrete at the zero iteration, we obtain:

$$q_{1,SG} = \frac{65.86 \cdot 0.67}{0.9^{1/2}\left(1+0.67\right)^2} ln \frac{200}{100} = 16.64 \cdot 0.6931 = 11.525 \text{ N/mm}.$$

To adequately compare the two analyzed concretes, the load on the cylinder of N concrete was reduced by the strength ratio between N and SG concrete.

$$q_{1,N} = \frac{35}{65.86} 11.525 = 6.123 \text{ N/mm}.$$

A static general step was employed to simulate the loading process. The monitored output parameters included hoop stress components. The radial stress components obtained from the analysis without porosity were used to determine the modified input parameters for the analysis with porosity. In this way, the effect of porosity on the long-term structural response was quantified. For SG concrete, the ABAQUS software provides results in the zero, first and second iterations. The second iteration is the last for this concrete because it reaches the ultimate strain of the concrete, which characterizes the fracture. For N concrete, the fracture occurs already in the first iteration. ABAQUS software therefore provides theoretical results for this concrete in the second and third iterations.

Figure 8 shows the ratios between the stresses at the failure surfaces under uniaxial compressive stresses on both concrete cylinders according to three laws: the MC law, the RDA prediction, and the DP criterion. The results show that the RDA prediction are in much better agreement with the DP criterion compared to the MC hypothesis, which deviates significantly. The same is true for the results for thick-walled concrete cylinders subjected to gradually increasing internal pressure under plane strain conditions and analyzed using the ABAQUS software.

Figure 9 shows the stress ratios for the calculated values of VVF. Compared to the results without the influence of porosity, the stress ratios are reduced because they are calculated at smaller internal friction angles. In this case, the solutions using the ABAQUS software for plane strain are in good agreement with the MC hypothesis in the case of uniaxial loading.

Figures 10 and 11 show the hoop stress diagrams during iterations along the cylinder thickness for both analyzed concretes. The hoop stresses reach peak values at the calculated elastic limits. The damage variables D_1 shown in Table 5 increase with iterations and shift the elasto-viscoplastic borders towards the outer radii, allowing the cylinders to yield at lower internal pressures.

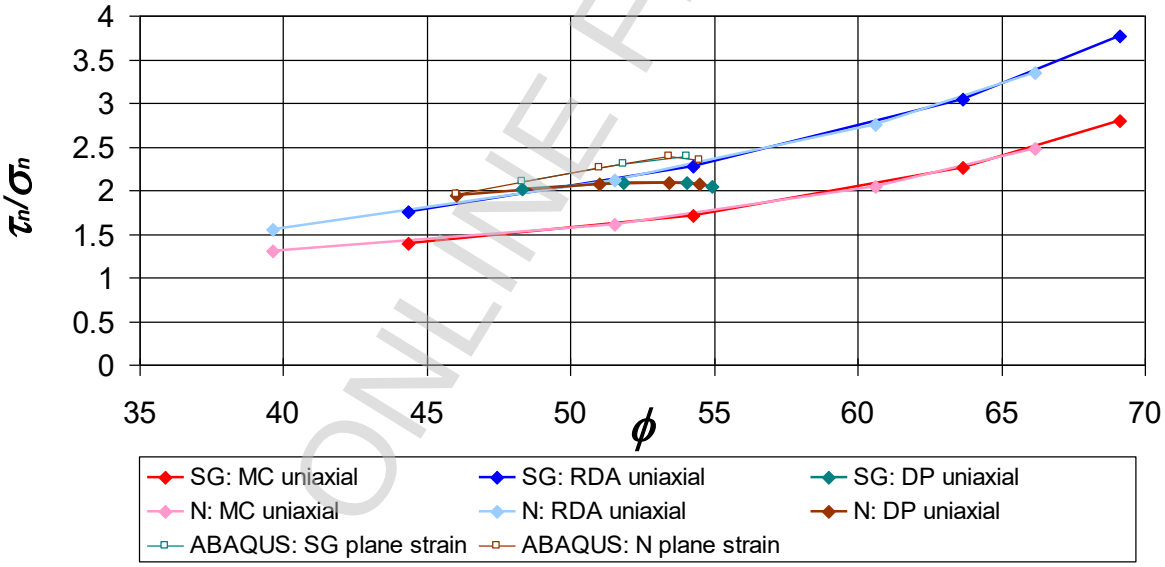


Figure 8. Ratios between the stresses at the fracture surfaces for both analyzed concretes and thick-walled concrete cylinders without the influence of porosity

ONLINE FIRST

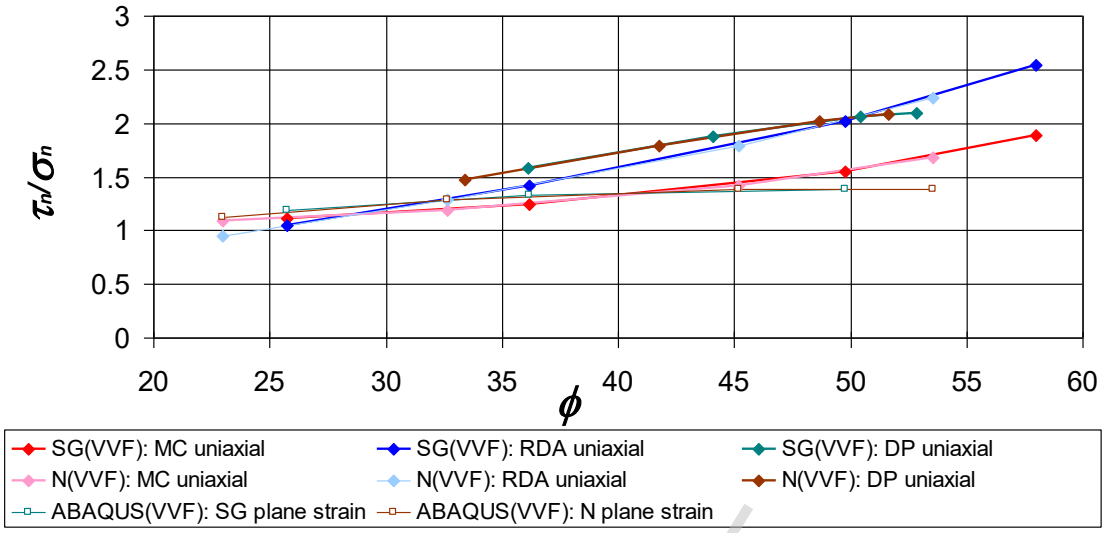


Figure 9. Ratios between the stresses at the fracture surfaces for both analyzed concretes and thick-walled concrete cylinders using the calculated values of the VVF

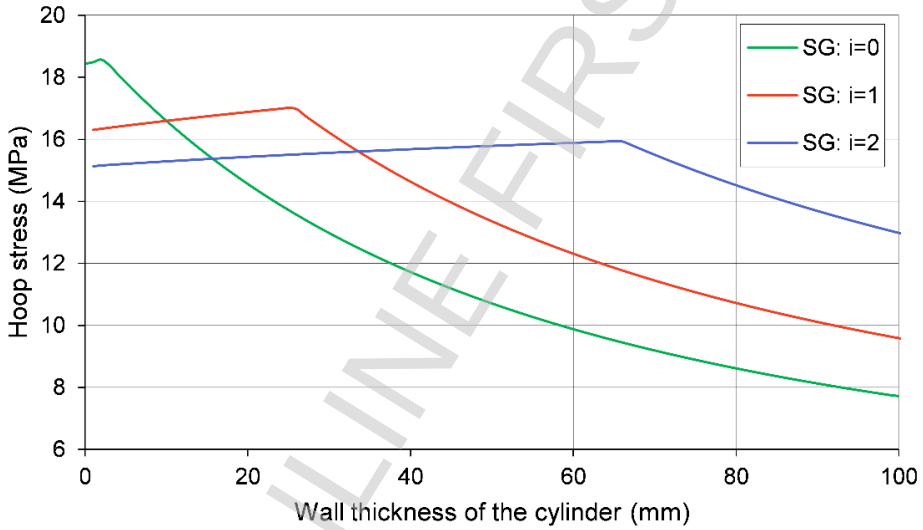
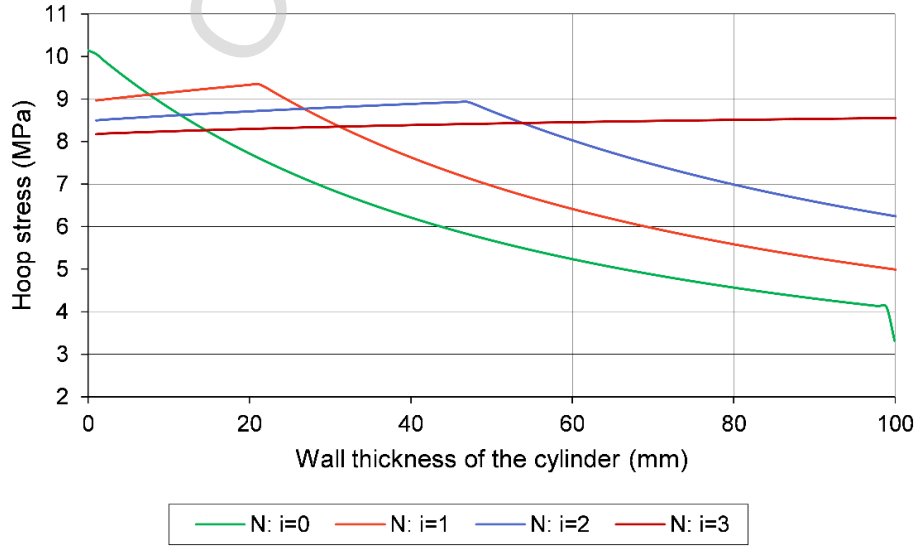


Figure 10. Hoop stresses over iterations for thick-walled cylinder made of SG concrete



ONLINE FIRST

Figure 11. Hoop stresses over iterations for thick-walled cylinder made of N concrete

Table 7 shows the results for the normal cohesive stresses $|S|$ given by [27] for the both analyzed concretes. It can be observed that normal cohesive stresses are in very good agreement with the hoop stresses σ_θ in thick-walled cylinders at their peak values calculated using the ABAQUS software. The differences are in the range of 0.5 to 4 percent.

The fact that the normal cohesive stresses represent the maximum hoop stresses at the elastic limits of thick-walled cylinders shows that the normal cohesive stresses derived using the RDA are relevant stresses using the fracture mechanics, [27].

Figures 12 and 13 display the hoop stress diagrams throughout the thickness of the cylinder for both types of analyzed concrete, considering the effect of VVF. The hoop stresses reach their maximum values at the calculated boundaries between the elastic and plastic zones.

The evolution of the hoop stress distribution provides additional insight into the deformation mechanism of the cylinder. At the zero iteration, the maximum hoop stress is located close to the inner surface, where plastic yielding first develops. In subsequent iterations stress redistribution within the cylinder causes the location of the maximum hoop stress to shift towards the outer radius. This redistribution is accompanied by a corresponding evolution of the elastic-plastic boundary.

When porosity is taken into account, the stress redistribution is further modified due to changes in the stiffness of the material. The difference in hoop stresses without and with the influence of porosity is not large, and the result is that by including porosity in each individual finite element, many of which remain within the elastic limits. Finite elements within the elastic limits have the lowest creep coefficients.

Table 7. Normal cohesive and hoop stresses for both analyzed thick-walled cylinders

Concrete	c_c (MPa)	ϕ (°)	$\|S\|$ (MPa)	σ_θ (MPa)	Diff. $\|S\|$ - σ_θ (%)
SG: i=0	25.508	44.331	18.25	18.57	1.72
SG: i=1	29.259	54.264	17.09	16.98	0.64
SG: i=2	36.368	63.663	16.13	15.92	1.3
SG: i=3	40.435	69.101	14.42	–	–
N: i=0	12.669	39.614	9.76	10.14	3.75
N: i=1	14.956	51.513	9.31	9.36	0.53
N: i=2	18.447	60.617	9.05	8.93	1.33
N: i=3	20.339	66.185	8.21	8.56	4.09

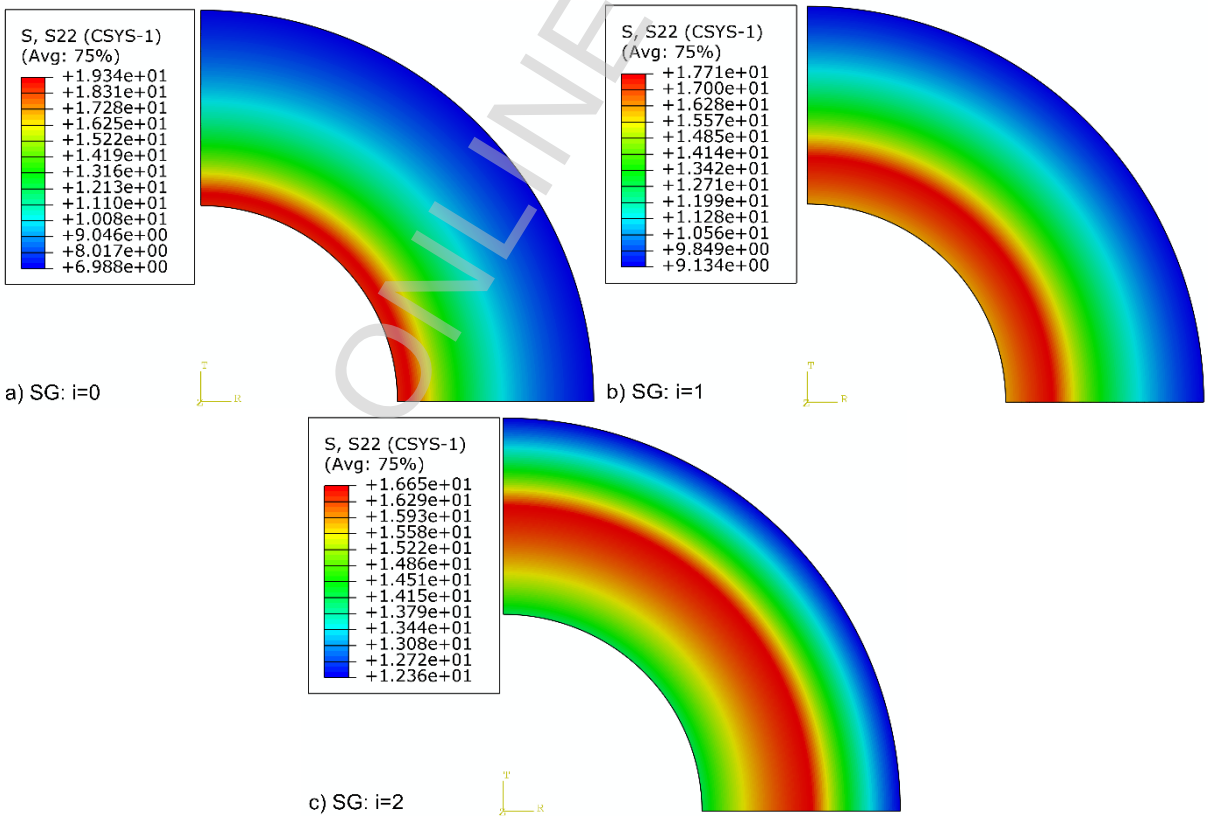


Figure 12. Hoop stresses with effect of VVF for thick-walled cylinder made of SG concrete: a) zero iteration; b) first iteration and c) second iteration

ONLINE FIRST

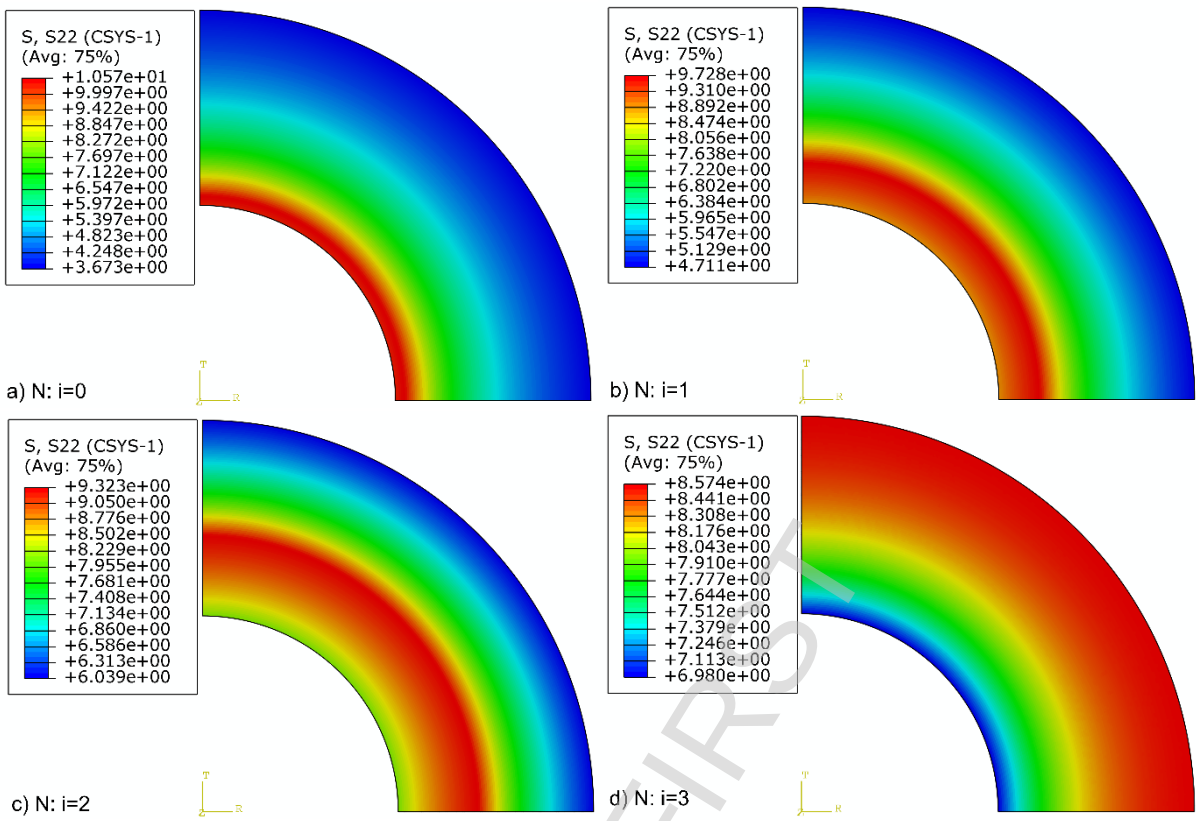


Figure 13. Hoop stresses with effect of VVF for thick-walled cylinder made of N concrete: a) zero iteration; b) first iteration, c) second iteration and d) third iteration

The introduction of porosity affects the evolution of the elastic-plastic boundary within the cylinder. At the zero iteration, the porous models exhibit an expansion of the plastic region compared with the non-porous cases for both SG and N concrete. With increasing iterations, the influence of porosity becomes more dependent on the material type. For SG concrete, the porous model results in a reduced plastic zone after the first iteration, indicating a more pronounced stress redistribution within the cylinder wall. The N concrete model at zero and first iteration shows a slightly larger plastic region, while at subsequent iterations the elastic-plastic boundary shifts towards the cylinder center, resulting in a reduction of the plastic zone. These differences indicate that porosity alters the stress redistribution within the cylinder, resulting in a different evolution of the plastic zone. Consequently, some elements that yielded in the non-porous model remain in the elastic regime when porosity is introduced.

The evolution of radial displacements is consistent with the observed changes in the elastic-plastic boundary. For SG concrete, the introduction of porosity results in lower radial displacements along the cylinder radius throughout all iterations. This behaviour is accompanied by a reduced extent of the plastic zone, indicating that stress redistribution caused by porosity modifies the deformation response of the cylinder. For N concrete, the influence of porosity on the deformation response is not uniform throughout the loading process. In zero iteration, the porous model exhibits both a larger plastic zone and higher radial displacements compared with the non-porous model. In the first loading iteration, although the plastic zone remains slightly larger, the radial displacements become lower than those of the non-porous model. This indicates that the extent of the plastic zone alone does not govern the displacement response.

4 Conclusions

This study aimed to extend the RDA framework by introducing an iterative procedure for analysing the inelastic behaviour of thick-walled concrete cylinders, with particular emphasis on the influence of porosity on hoop stresses, radial displacements, and the elasto-viscoplastic boundary. The proposed approach combines RDA iterations with the DP yield criterion and FEM implemented in ABAQUS, with a complete FEM performed at each iteration. This procedure enables the effects of evolving material parameters and element-wise porosity to be investigated, as well as their influence on the predicted structural response at successive stages of the analysis. The study further examines the differences between porous and non-porous configurations to assess the role of porosity in the inelastic behaviour of concrete cylinders.

The results indicate that the key parameter in predicting the behavior of concrete over its expected service life is the creep coefficient, which increases with time or in increasing iterations. This refers to the behavior of concrete during strain hardening. Concrete exhibits ductile behavior above the yield point until failure. In this range, RDA provides solutions close to the DP yield criterion for associated flow. The influence of porosity is reflected at reduced angles of internal friction, when the material exhibits brittle behavior. In this range, the DP criterion approaches the MC hypothesis. These findings demonstrate the relevance of the selected

IN PRESS ARTICLE IN PRESS

yield criterion to the material response represented by the RDA model.

Within the adopted RDA framework, when a material has porosity, the bulk compressibility modulus and shear modulus are no longer constants, but functions of the pore geometry. RDA views the change in porosity as a process of energy dissipation within a solid matrix. By analogy, the energy that would be lost to damping in a dynamic system is spent in a real material on micro-splattering and the generation of new free surfaces (increasing porosity thresholds). As porosity increases and approaches a critical point – the maximum VVF (percolation threshold) – the bulk compressibility modulus drops drastically. At the moment when the strain energy density drops to zero, the material loses its ability to store elastic energy. This point numerically defines the maximum VVF before the complete collapse of the internal structure.

The numerical results obtained through the chosen implementation approach in the ABAQUS software - which utilizes discrete points (the zeroth, first, second, and third iterations from the 1D RDA method) - offer an exceptionally elegant way to bypass the "Cap" model, which is computationally demanding and often numerically unstable. By entering these points directly, we actually force the base of the DP cone to expand in 3D space as dictated by RDA iterations. Cylinders also exhibit ductile behavior in the VEP range above the yield point. Larger damage variables shift the elasto-viscoplastic boundary toward the outer radius of the cylinder. Porosity was included in the analysis by previously determining the VVF value at the level of each finite element in the mesh. VVF values are determined via porosity thresholds resulting from different strain energy densities based on positive and negative values of dynamic Poisson's ratios. Higher porosity thresholds in increasing iterations shift the EVP boundary towards the outer radius of the cylinder.

The main result in the analysis of thick-walled cylinders is that the hoop stress is actually a normal cohesive stress shown in Table 7. The maximum values of the hoop stress are at the elastic limits of the material. The influence of porosity is reflected in slightly higher hoop stresses and elastic limits that are shifted towards the inner edges of the cylinder. The greatest influence of porosity is on radial displacements, which are significantly reduced because a large number of finite elements remain in the elastic regions of the cylinder where the influence of porosity is significantly reduced.

The principal methodological novelty of this study is the introduction of an iterative procedure within the RDA framework, involving a complete FEM at each iteration, and its application to porous, thick-walled concrete cylinders. The proposed approach enables a systematic investigation of hoop stresses, interpreted within the RDA framework as normal cohesive stresses, and their relationship with creep, porosity, and inelastic deformation. By examining iterations together with the element-wise distribution of porosity, the study evaluates the effects of these factors on hoop-stress distributions, radial displacements, and the position of the elasto-viscoplastic boundary. The findings extend the application of the RDA framework to the iterative analysis of porous concrete cylinders and provide further insight into the role of cohesive stresses in their inelastic behaviour.

Author contribution statement

D.D.M. contributed to the conceptualization and development of the methodology, and performed the analysis. D.D.M. and N.M.B. contributed to the analysis of the software-generated data, while N.M.B. was responsible for the software implementation. D.D.M. prepared the first version of the manuscript. D.D.M. and N.M.B. jointly contributed to the subsequent development, review, and editing of the manuscript. All authors reviewed and approved the final manuscript.

Conflicts of Interest

The authors declare no conflicts of interest.

Acknowledgments

This research received no external funding.

References

[1] M. Reiner, Building Materials, Their Elasticity and Inelasticity, North-Holland Publishing Company, Amsterdam, 1954.

[2] M. Reiner, Plastic yielding in anelasticity, J. Mech. Phys. Solids 8 (1960) 255–261. https://doi.org/10.1016/0022-5096(60)90030-2.

[3] O.C. Zienkiewicz, Cormeau I.C, Visco-Plasticity solution by finite element process, Arch. Mech. 24 (1972) 873–889.

[4] O.C. Zienkiewicz, D.R.J. Owen, I.C. Cormeau, Analysis of viscoplastic effects in pressure vessels by the finite element method, Nucl. Eng. Des. 28 (1974) 278–288. https://doi.org/10.1016/0029-5493(74)90037-5.

[5] D.R.J.. Owen, E.. Hinton, Finite elements in plasticity : theory and practice, Pineridge Press, Swansea, U.K, 1980.

[6] Cormeau, Numerical stability in quasi-static elasto/visco-plasticity, Int. J. Numer. Methods Eng. 9 (1975) 109–127. https://doi.org/10.1002/NME.1620090110.

[7] T.J.R. Hughes, R.L. Taylor, Unconditionally stable algorithms for quasi-static elasto/visco-plastic finite element analysis, Comput. Struct. 8 (1978). https://doi.org/10.1016/0045-7949(78)90019-6.

[8] D.R.J. Owen, A. Prakash, O.C. Zienkiewicz, Finite element analysis of non-linear composite materials by use of overlay systems, Comput. Struct. 4 (1974). https://doi.org/10.1016/0045-7949(74)90035-2.

[9] G.N. Pande, D.R.J. Owen, O.C. Zienkiewicz, Overlay models in time-dependent non-linear material analysis, Comput. Struct. 7 (1977). https://doi.org/10.1016/0045-7949(77)90080-3.

[10] W.F. Chen, Plasticity in reinforced concrete, McGraw-Hill, New York, 1982.

[11] W.F. Chen, D.J. Han, Plasticity for Structural Engineers, Springer-Verlag, New York, 1988. https://doi.org/10.1007/978-1-4612-3864-5.

[12] A. Dummer, M. Neuner, G. Hofstetter, An extended gradient-enhanced damage-plasticity model for concrete considering nonlinear creep and failure due to creep, Int. J. Solids Struct. 243 (2022) 111541. https://doi.org/10.1016/J.IJSOLSTR.2022.111541.

[13] X. Ren, Q. Wang, R. Ballarini, X. Gao, Coupled Creep-Damage-Plasticity Model for Concrete under Long-Term Loading, J. Eng. Mech. 146 (2020) 04020027. https://doi.org/10.1061/(ASCE)EM.1943-7889.0001748.

[14] Z.P. Bažant, M. Jirásek, Creep and hygrothermal effects in concrete structures, Solid Mech. Its Appl. 225 (2018) 1–921. https://doi.org/10.1007/978-94-024-1138-6/COVER.

ONLINE FIRST

[15] Y. Zhang, T. Sun, M. Qin, D. Zhang, N. Qin, Y. Wang, Effect of Time and Stress on Creep Damage Characteristics of Cement-Based Materials, Build. 2024, Vol. 14, Page 3745 14 (2024) 3745. https://doi.org/10.3390/BUILDINGS14123745.

[16] D.D. Milašinović, The finite strip method in computational mechanics, Faculties of Civil Engineering: University of Novi Sad, Technical University of Budapest and University of Belgrade: Subotica, Budapest, Belgrade, 1997. https://books.google.ba/books/about/The_Finite_Strip_Method_in_Computational.html?id=chlbAAAACAAJ&redir_esc=y (accessed February 6, 2019).

[17] D.D. Milašinović, Rheological-dynamical analogy: Modeling of fatigue behavior, Int. J. Solids Struct. 40 (2003) 181–217. https://doi.org/10.1016/S0020-7683(02)00518-8.

[18] E. Liu, S. He, Effects of cyclic dynamic loading on the mechanical properties of intact rock samples under confining pressure conditions, Eng. Geol. 125 (2012). https://doi.org/10.1016/j.enggeo.2011.11.007.

[19] D.D. Milašinović, Rheological-dynamical method for prediction of compressive strength and deformation of rocks, Int. J. Rock Mech. Min. Sci. 141 (2021) 104659. https://doi.org/10.1016/j.ijrmms.2021.104659.

[20] N.W. Tschoegl, W.G. Knauss, I. Emri, Poisson's ratio in linear viscoelasticity - a critical review, Mech. Time-Dependent Mater. 6 (2002) 3–51. https://doi.org/10.1023/A:1014411503170.

[21] R. Lakes, Foam structures with a negative poisson's ratio, Science (80-.). 235 (1987) 1038–1040. https://doi.org/10.1126/science.235.4792.1038.

[22] R.S. Lakes, A. Wineman, On Poisson's ratio in linearly viscoelastic solids, J. Elast. 85 (2006) 45–63. https://doi.org/10.1007/s10659-006-9070-4.

[23] R.J. Bathurst, L. Rothenburg, Note on a random isotropic granular material with negative Poisson's ratio, Int. J. Eng. Sci. 26 (1988) 373–383. https://doi.org/10.1016/0020-7225(88)90116-4.

[24] S. Murakami, Continuum damage mechanics, Springer Science+Business Media B.V, 2012. https://doi.org/10.1007/978-94-007-2666-6.

[25] D.D. Milašinović, Rheological-dynamical continuum damage model for concrete under uniaxial compression and its experimental verification, Theor. Appl. Mech. 42 (2015) 73–110. https://doi.org/10.2298/tam1502073m.

[26] D.C. Drucker, W. Prager, Soil mechanics and plastic analysis or limit design, Q. Appl. Math. 10 (1952) 157–165. https://doi.org/10.1090/qam/48291.

[27] D.D. Milašinović, Rock failure mechanisms based on rheological dynamics, J. Rock Mech. Geotech. Eng. 17 (2025) 2239–2255. https://doi.org/10.1016/j.jrmge.2024.04.036.

[28] D.D. Milašinović, Modeling of porous-hardened concrete by rheological-dynamical analogy, Eng. Comput. (Swansea, Wales) 40 (2023) 2615–2647. https://doi.org/10.1108/EC-08-2022-0574/FULL/XML.

[29] X. Chen, D. Shi, S. Guo, Experimental Study on Damage Evaluation, Pore Structure and Impact Tensile Behavior of 10-Year-Old Concrete Cores After Exposure to High Temperatures, Int. J. Concr. Struct. Mater. 14 (2020) 1–17. https://doi.org/10.1186/s40069-020-0393-5.

[30] L. Xu, Y. Duan, Y. Li, Porosity, gradient and impact velocity effects on compressive response of foamed concrete, Constr. Build. Mater. 315 (2022) 125616. https://doi.org/10.1016/J.CONBUILDMAT.2021.125616.

[31] P.H. Mott, C.M. Roland, Limits to Poisson's ratio in isotropic materials, Phys. Rev. B - Condens. Matter Mater. Phys. 80 (2009) 132104. https://doi.org/10.1103/PhysRevB.80.132104.

[32] D.D. Milašinović, D. Goleš, L. Kozarić, S. Bursać, N. Mrđa Bošnjak, J. Gučević, A. Pančić, Porosity Effects on Folded-Plate Structures by Finite Strip Method and Rheological Dynamics, Int. J. Civ. Eng. 23 (2025) 895–913. https://doi.org/10.1007/s40999-024-01065-x.

[33] N. Mrđa Bošnjak, D.D. Milašinović, D. Goleš, J. Gučević, A. Čeh, Porosity Effects on the Composite Girder by Rheological Dynamics and FEM, Materials (Basel). 17 (2024) 5779. https://doi.org/10.3390/ma17235779.

[34] W. Ramberg, W.R. Osgood, Description of stress-strain curves by three parameters, Natl. Advis. Comm. Aeronaut. (1943) Technical Note No. 902.

[35] D.D. Milašinović, Rheological–dynamical analogy: visco-elasto-plastic behavior of metallic bars, Int. J. Solids Struct. 41 (2004) 4599–4634. https://doi.org/10.1016/j.ijsolstr.2004.02.061.

[36] D.D. Milašinović, Fatigue crack growth and failure of inelastic rods based on rheological-dynamical analogy, Int. J. Fatigue 33 (2011) 372–381. https://doi.org/10.1016/j.ijfatigue.2010.09.011.

[37] D.D. Milašinović, A. Landović, Rheological-dynamic model for load-bearing capacity of composite columns due to concrete core failure, Mater. Struct. 56 (2023) 75. https://doi.org/10.1617/s11527-023-02163-3.

[38] M. Johansson, K. Gylltoft, Mechanical Behavior of Circular Steel–Concrete Composite Stub Columns, J. Struct. Eng. 128 (2002) 1073–1081. https://doi.org/10.1061/(asce)0733-9445(2002)128:8(1073).

[39] C. Müller, Beton als kreislaufgerechter Baustoff, Schriftenreihe des Deutschen Ausschuss für Stahlbeton, DAfStb, Berlin, Beuth Verlag, 2001.

[40] D.D. Milašinović, D. Goleš, A. Pančić, A. Čeh, Rheological-dynamical model of concrete and its application on RC beams, Mech. Time-Dependent Mater. 26 (2022). https://doi.org/10.1007/s11043-020-09476-8.

[41] J. Lemaitre, J. Dufailly, Damage measurements, Eng. Fract. Mech. 28 (1987) 643–661. https://doi.org/10.1016/0013-7944(87)90059-2.

[42] S.H. Goods, L.M. Brown, Overview No. 1: The nucleation of cavities by plastic deformation, Acta Metall. 27 (1979) 1–15. https://doi.org/10.1016/0001-6160(79)90051-8.

[43] A. Needleman, V. Tvergaard, An analysis of ductile rupture in notched bars, J. Mech. Phys. Solids 32 (1984) 461–490. https://doi.org/10.1016/0022-5096(84)90031-0.

[44] J. Lemaitre, How to use damage mechanics, Nucl. Eng. Des. 80 (1984) 233–245. https://doi.org/10.1016/0029-5493(84)90169-9.

[45] ABAQUS. Theory Manual and User's Manual. In.: Dassault System Simulia Corp, Providence, RI, USA, 2012.

ONLINE FIRST